Single crystal growth and thermoelectric properties of Nowotny chimney-ladder compound Fe_2Ge_3

Youming Xu [1], Yan Wu [2], Huibo Cao [2], Shucheng Guo [1], Jiaqiang Yan [3,*] and Xi Chen [1,†]

[1]*Department of Electrical and Computer Engineering, University of California Riverside, Riverside, California 92501, USA*

[2]*Neutron Scattering Division, Oak Ridge National Laboratory, Oak Ridge, Tennessee 37831, USA*

[3]*Materials Science and Technology Division, Oak Ridge National Laboratory, Oak Ridge, Tennessee 37831, USA*

(Received 14 June 2023; revised 3 November 2023; accepted 28 November 2023; published 22 December 2023)

Fe_2Ge_3 with an incommensurate Nowotny chimney-ladder (NCL) structure is a promising material for thermoelectric applications due to its low thermal conductivity. Previous experimental studies on Fe_2Ge_3 have mainly focused on polycrystalline samples, resulting in a limited understanding of the material's intrinsic thermoelectric properties and the underlying causes of its low thermal conductivity. Here we report the synthesis and thermoelectric properties of single crystalline Fe_2Ge_3. Millimeter-sized Fe_2Ge_3 single crystals grown by the chemical vapor transport method enable the study of the intrinsic thermoelectric properties. The Seebeck coefficient of Fe_2Ge_3 is negative and its magnitude increases linearly with temperature, showing a degenerate *n*-type semiconductor behavior. Analysis of the electrical resistivity and specific heat data indicates the existence of an Einstein mode with a characteristic temperature of about 60 K, suggesting the presence of low-energy optical phonons. The thermal conductivity of Fe_2Ge_3 along the *c* axis is as low as $1.9\,W\,m^{-1}\,K^{-1}$ at 300 K and exhibits a nearly temperature-independent characteristic, which is distinct from the previous theoretical calculations with a stronger temperature dependence. The low thermal conductivity may be attributed to the scattering of acoustic phonons by low-energy optical modes and the presence of non-extended diffuson modes, as reported in another NCL compound, $MnSi_{1.74}$. This study provides valuable insights into the electrical and thermal properties of Fe_2Ge_3, which can open up possibilities for future advances in thermoelectric applications.

DOI: 10.1103/PhysRevMaterials.7.125404

I. INTRODUCTION

Solid-state thermoelectric (TE) devices, which can directly convert waste heat into electricity and vice versa, have received renewed attention in recent decades [1–3]. The performance of a TE device is mainly determined by the dimensionless figure of merit of a TE material as $zT = S^2T/\rho\kappa$, where S, T, ρ, and κ are the Seebeck coefficient, temperature, electrical resistivity, and thermal conductivity, respectively. The product of S^2/ρ is called the power factor (*PF*). The thermal conductivity comprises two components, the lattice contribution (κ_L) and the electronic thermal contribution (κ_E). The search for alternative TE materials is dominated by the need to minimize the κ_L while maximizing their *PF*. [4–9]

Many efforts have been devoted to exploring novel materials with complex crystal structures. [10–15] For example, Nowotny chimney-ladder (NCL) compounds T_mE_n, which consist of transition (T) and main group (E) metals, are promising TE materials due to their intrinsically low thermal conductivity as a result of complex crystal structures. [16,17] The unit cell of a NCL phase consists of a tetragonal sublattice forming chimneys and a helical sublattice forming ladders. The periodicities of the two sublattices along the *c* axis are in general incommensurate with respect to each other. Examples of NCL phases include $MnSi_{1.74}$, Ru_2Si_3, $RuAl_2$, Ru_2Ge_3, and so on. [18–21] These NCL compounds usually exhibit low κ values, ranging from 0.8 to $4.2\,W\,m^{-1}\,K^{-1}$ at 300 K. The reported figure of merit zT is in the range of 0.1–1.0. [22–24] To understand the origin of low thermal conductivity in $MnSi_{1.74}$, Chen *et al.* [10] conducted inelastic neutron scattering measurements and first-principles calculations to determine the phonon dispersions. These experiments revealed numerous low-energy optical phonon modes in $MnSi_{1.74}$, including an unusual twisting mode of Si ladders, which can scatter acoustic modes and lead to an intrinsically low κ. Furthermore, a hybrid model consisting of both phonons and diffusons was proposed to explain the low and anisotropic thermal conductivity of $MnSi_{1.74}$. [10]

Fe_2Ge_3 is a NCL compound in the Fe-Ge binary system. Gerasimov and Pavlov [25] prepared an equilibrium phase Fe_2Ge_3 by mechanical alloying followed by annealing. This new phase shows a tetragonal structure similar to Ru_2Sn_3. Li *et al.* [26] studied the postannealed Fe-Ge alloy by x-ray diffraction (XRD) and transmission electron microscopy. Its composition was determined as $FeGe_{1.52}$, slightly different from the Ru_2Sn_3-type structure, which was attributed to formation of incommensurate structure. Terada *et al.* [27] grew the epitaxial $FeGe_{1.52}$ thin film via the seed-assisted epitaxial method and the orientation of the helices was controlled by nanoseed interfaces. Sato *et al.* [28] characterized the TE properties of a polycrystalline Fe_2Ge_3 sample prepared by mechanical alloying followed by spark plasma sintering. A maximum zT of 0.57 was achieved at 633 K as a result of a low lattice thermal conductivity of $1\,W\,m^{-1}\,K^{-1}$. Li *et al.* [29]

*yanj@ornl.gov
†xichen@ucr.edu

calculated the lattice thermal conductivity of Fe_2Ge_3 and discussed the effect of optical-acoustic phonon hybridization on phonon scattering. The hybridization increases the scattering rate of acoustic phonons, leading to low thermal conductivity. Recently, Verchenko *et al.* [30] reported the crystal growth of Fe_2Ge_3 via a chemical vapor transport (CVT) method using a mixture of I_2 and $Mo(CO)_6$ as transport agents and obtained crystals with typical sizes in the range of 100–750 microns. It should be noted that these crystals are not large enough for the TE property measurements. Previous studies on the TE properties are mainly focused on polycrystalline samples. Hence it is of interest to explore the intrinsic transport properties of Fe_2Ge_3 single crystals.

Herein, we report the synthesis and transport properties of Fe_2Ge_3 single crystals, which were prepared by a CVT method using I_2 as a transport agent. Single crystals of Fe_2Ge_3 with relatively large sizes, reaching up to 3 mm, were successfully obtained. The TE and magnetic properties of Fe_2Ge_3 were characterized. The resistivity of Fe_2Ge_3 increases with temperature and starts to decrease above 300 K. A fitting of resistivity and specific heat (C_p) reveals an Einstein mode with a characteristic temperature (θ_E) of about 60 K, suggesting the existence of low-energy optical modes. The Seebeck coefficient of Fe_2Ge_3 is negative and its magnitude increases linearly with temperature, which is typical for a degenerate *n*-type semiconductor. Furthermore, the thermal conductivity of Fe_2Ge_3 along the *c* axis shows a temperature-independent behavior with a low value of $1.9\,W\,m^{-1}\,K^{-1}$ at 300 K, possibly due to the scattering of acoustic phonons by low-energy optical modes. Additionally, the temperature-independent magnetic susceptibility could be attributed to Pauli paramagnetism by conduction electrons. This study provides useful insights into the intrinsic physical properties of Fe_2Ge_3 and the origin of its low thermal conductivity.

II. EXPERIMENTAL METHODS

A. Crystal growth of Fe_2Ge_3

Fe_2Ge_3 single crystals were grown by the CVT technique using I_2 as the transport agent. First, Fe (99.99%, Alfa Aesar) and Ge (99.9999%, Alfa Aesar) pieces in the atomic ratio of 2:3 were arc melted to get a uniform mixture. Then, the mixture and transport agent ($4\,mg\,cm^{-3}$) were sealed under vacuum (10^{-5} Torr) inside a quartz tube. The vapor transport growth was performed in a single zone tube furnace by using the natural temperature gradient along the horizontal axis. The starting materials were heated for 2 weeks at $T_{hot} = 500\,^{\circ}C$, whereas the other end of the tube that did not contain the precursors was maintained at $T_{cold} = 460\,^{\circ}C$. During the 2-week growth period, some black plates form around the starting materials at the hot end. These plates are rather moisture sensitive. We failed to confirm the real chemistry of these crystals. However, FeI_2 is expected to form with a layered structure and to be rather moisture sensitive. It is likely that I_2 reacts with iron to form FeI_2 which then serves as the transport agent during the crystal growth. The Fe_2Ge_3 crystals show up at the cold end as the rectangular bars with a typical length of 2–3 mm and cross section of $0.5 \times 0.6\,mm^2$.

B. Phase and microstructure characterization of Fe_2Ge_3

Room temperature powder x-ray diffraction patterns were collected on an X'Pert PRO MPD x-ray powder diffractometer using Ni-filtered Cu Kα radiation with a wavelength of 1.54 Å. The crystal facet indexing was carried out using a Bruker Venture D8 diffractometer equipped with a Photon III detector. The single crystal XRD (SCXRD) was collected on a Rigaku x-ray diffractometer using Mo Kα radiation with a wavelength of 0.71073 Å at 298 K. The elemental composition and morphology of the samples were studied using a TESCAN Vega3 SBH scanning electron microscope (SEM) with a Bruker LN_2-free $30\,mm^2$ SD detector. The energy dispersive x-ray (EDX) analysis utilized Fe Kα and Ge Lα for elemental quantitative analysis. The transmission electron microscope (TEM) study was performed with a Thermo Fisher Scientific Talos L120C TEM with an FEI CETA-16 M CMOS digital camera. The Raman spectrum was obtained via Horiba LabRAM using a laser with a wavelength of $520\,cm^{-1}$ and a maximum power of 60 mW at 300 K. The incident laser beam is nonpolarized and oriented perpendicular to the *c* axis of the crystal.

C. Thermoelectric and magnetic measurements of Fe_2Ge_3

The magnetic properties of samples were measured with a Quantum Design (QD) Magnetic Property Measurement System (MPMS) in the temperature interval $2\,K \leqslant T \leqslant 350\,K$. The temperature dependence of specific heat was measured with a QD Physical Property Measurement System (PPMS) in the temperature range of $1.9\,K \leqslant T \leqslant 250\,K$. The Hall carrier concentration (n_H) and Hall mobility (μ_H) were measured using the PPMS with a magnetic field between $\pm 2\,T$. A single band model [31] was used to determine the charge carrier concentration and mobility of the samples. The carrier concentration is calculated using the formula $n_H = 1/(eR_H)$ and the Hall mobility is calculated using the formula $\mu_H = 1/(\rho e n_H)$, where e is the electron charge, R_H is Hall resistivity, and ρ is electrical resistivity. The electrical resistivity along the *c* axis was measured in the range of 2–380 K using the PPMS. The Seebeck coefficient data along the *c* axis were collected in a homemade setup from 80 to 310 K. The thermal conductivity along the *c* axis was measured in the temperature interval between 30 and 300 K by the steady-state method. [32] The differential thermocouple was made of copper and Constantan wires.

III. RESULTS AND DISCUSSION

A. Crystal structure

The crystal structure of Fe_2Ge_3 is shown in Fig. 1(a). Fe_2Ge_3 exhibits a NCL structure with a space group of $P\bar{4}c2$ (No. 116). [28,30] Similar to other NCL phases, Fe_2Ge_3 consists of a tetragonal sublattice of Fe atoms forming chimneys and a tetragonal sublattice of Ge atoms forming ladders. These two sublattices are not necessarily commensurate along the *c* axis. Its composition can slightly deviate from the Fe:Ge=2:3. [28,30,33] The indexed room-temperature powder XRD pattern is displayed in Fig. 1(b). All the reflections can be indexed using space group $P\bar{4}c2$ (No.116) and no impurities were detected by XRD. It should be noted that the (100) peak shows

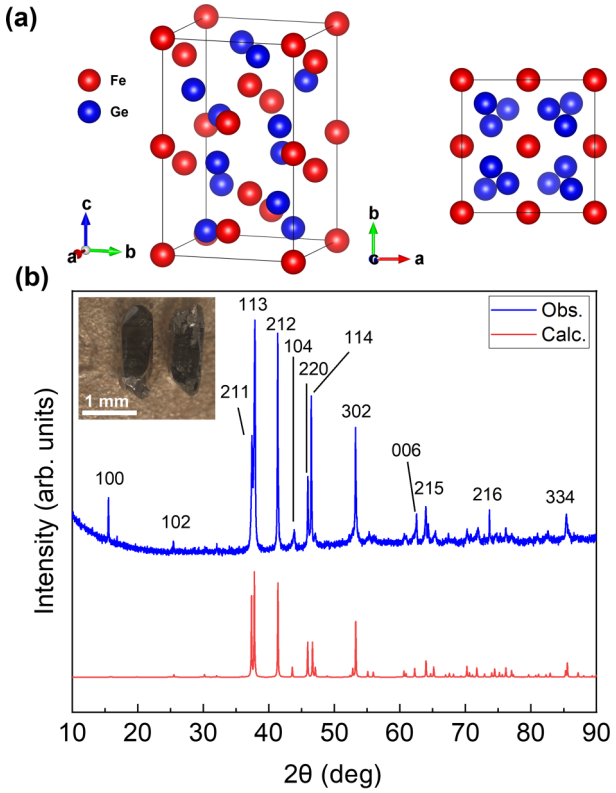

FIG. 1. (a) Crystal structure of NCL phase of Fe_2Ge_3. The red and blue spheres are Fe and Ge atoms, respectively. (b) Indexed powder XRD pattern (blue) of Fe_2Ge_3 compared with the calculated XRD pattern (red) based on the space group of $P\bar{4}c2$. The inset shows an optical image of as-grown crystals.

a higher intensity than the calculated XRD, which could be attributed to the presence of both commensurate and incommensurate structures as reported in a previous study [30], or to the influence of the texture effect [34]. The obtained lattice parameters from SCXRD are $a = b = 5.5995(6)$ Å and $c = 8.9531(14)$ Å, which are in good agreement with the reported values. [30,33] The single crystal crystallographic report and structure refinement results from SCXRD are listed in Tables I and II.

Figure 2(a) shows the SEM image of Fe_2Ge_3 single crystals. The single crystals typically display a cuboid shape, with

TABLE I. Single crystal crystallographic data and structure refinement for Fe_2Ge_3 at 298 K.

Space group	$P\bar{4}c2$
Lattice parameters	$a = b = 5.5995(6)$ Å, $c = 8.9531(14)$ Å
	$\alpha = \beta = \gamma = 90^\circ$
	$V = 280.73(6)$ Å^3
Density	7.848 g cm^{-3}
Temperature	298.00 K
Range for data collection	4.34°–31.40°
Collected reflections	1434 (total), 261 (unique)
R_{int}	0.0596
$\sigma I/I$	0.0694

TABLE II. Atomic coordinates data for Fe_2Ge_3 from SCXRD refinement with FULLPROF [35]. The reliability parameters of refinement are $\chi^2 = 4.72$ and $R_{factor} = 8.47\%$.

No.	Site	Wyckoff	x	y	z	Occupancy
1	Fe1	2b	0.5	0.5	0.25	0.25
2	Fe2	2c	0	0	0	0.25
3	Fe3	4i	0	0.5	0.37367(93)	0.5
4	Ge1	4f	0.17671(59)	0.17671(59)	0.75	0.501(6)
5	Ge2	8i	0.22206(71)	0.34436(62)	0.08555(58)	1.013(11)

widths in the range of a few hundred microns and lengths that can extend up to 3 mm. They also exhibit a distinct preferred growing direction. To determine the growth direction, we performed crystal facet indexing using SCXRD. It has been confirmed that the growth direction of the crystals is along the c axis, as shown in Fig. S1 in the Supplemental Material (SM). [36] The EDX spectrum of the sample is shown in Fig. 2(b). The EDX analysis indicates that the atomic ratio of Fe:Ge is $1 : 1.48 \pm 0.30$, which is consistent with the nominal atomic ratio of Fe_2Ge_3. Additionally, the EDX mapping of Fe and Ge elements confirms the homogeneity of the sample, as shown in Figs. 2(c) and 2(d).

To further investigate the crystal structure, we performed TEM studies on a Fe_2Ge_3 crystal. Figure 3(a) shows the high-resolution TEM (HRTEM) image of a sample. The interplanar spacing was measured to be 4.6 Å, consistent with the calculated d spacing of the $(10\bar{1})$ plane for the commensurate phase of Fe_2Ge_3 (4.6 Å). [30] The fast Fourier transform (FFT) pattern from the HRTEM image [inset of Fig. 3(a)] and selected area electron diffraction (SAED) [Fig. 3(b)] can be indexed based on the commensurate phase with the zone axis along the [121] direction. According to a previous study [30], both commensurate and incommensurate phases can exist in Fe_2Ge_3 crystals grown by the CVT method. Therefore, it is expected that a mixture of commensurate and incommensurate phases may also be present in our samples.

The Raman spectrum of a Fe_2Ge_3 sample is shown in Fig. S2 [36] with a peak at 147 cm^{-1}, corresponding to an energy of 18 meV. However, no other well-defined Raman peaks can be observed in the measured energy range. It should be noted that further studies, such as first-principles calculations, are needed to better understand the optical property of Fe_2Ge_3.

B. Magnetic property

Temperature dependence of the magnetic susceptibility (χ) of Fe_2Ge_3 single crystals was measured in a magnetic field of 10 kOe, as displayed in Fig. 4. A temperature-independent magnetic susceptibility of about 3×10^{-4} emu mol^{-1} Oe^{-1} was observed in the whole temperature range of 2–350 K. The nearly temperature-independent positive magnetic susceptibility could be characterized by Pauli paramagnetism from conduction electrons. The electrical property measurements below confirm the metallic nature of the compound with temperature-independent carrier concentration. According to partial density of states and the electronic structure of Fe_2Ge_3 calculated by Verchenko *et al.*, [30] the valence band top

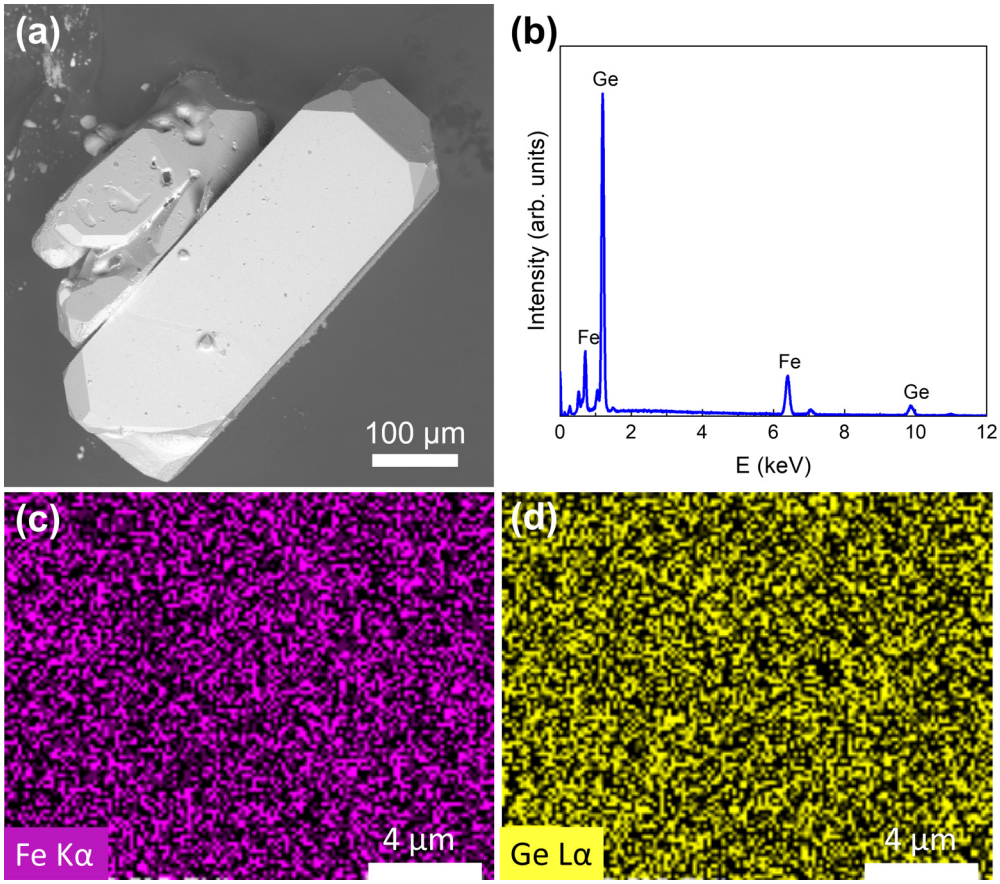

FIG. 2. (a) SEM image of the Fe_2Ge_3 single crystals. (b) EDX spectrum of the Fe_2Ge_3 single crystals. (c), (d) EDX mapping of Fe and Ge elements.

is mainly contributed by Ge 4*p* states while the conduction band bottom is contributed by Fe 3*d* states. Therefore, the paramagnetic properties should be attributed to Fe 3*d* and Ge 4*p* orbitals. The magnetic susceptibility shows weak anisotropy when the magnetic field is applied along and perpendicular to the *c* axis, as shown in Fig. S3 of the SM [36]. Previous results from Verchenko *et al.* [30] detected an upturn below 50 K and attributed it to paramagnetic impurities.

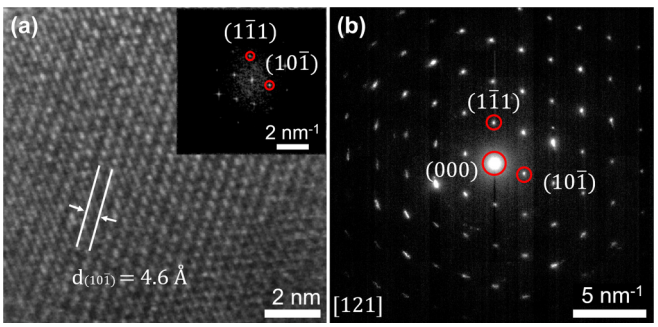

FIG. 3. (a) HRTEM image of a Fe_2Ge_3 single crystal. The corresponding FFT of the HRTEM is shown in the inset. (b) SAED pattern along zone axis [121], indexed based on the commensurate phase of Fe_2Ge_3.

C. Electrical properties

Figure 5(a) shows the temperature dependence of resistivity of two Fe_2Ge_3 single crystals measured with the electrical current along the *c* axis. The resistivity of Fe_2Ge_3 increases with increasing temperature and starts to decrease above 300 K. The resistivity at 300 K is 0.07 Ω cm with the residual

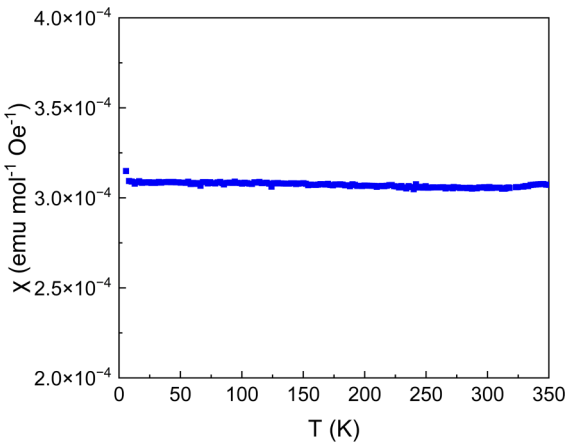

FIG. 4. Temperature dependence of magnetic susceptibility of Fe_2Ge_3 measured in an applied magnetic field of 10 kOe along a random orientation of one piece of crystal about 6 mg.

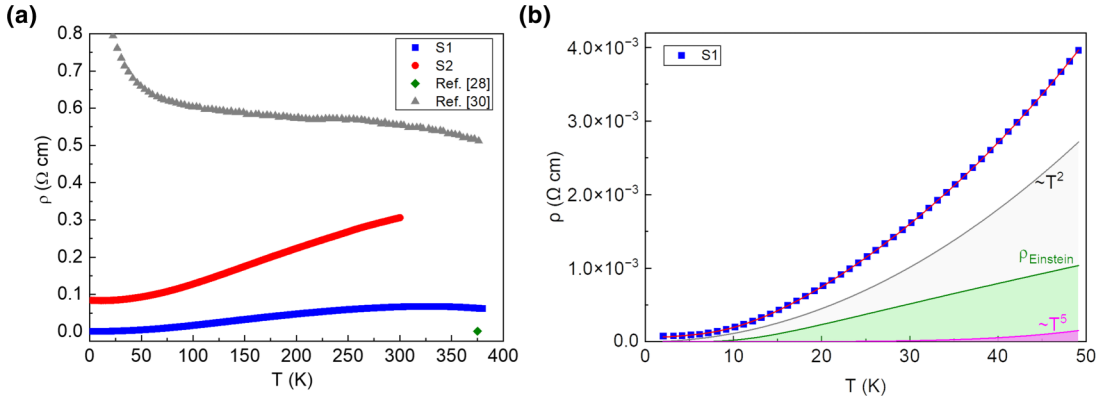

FIG. 5. (a) Temperature dependence of resistivity of Fe_2Ge_3 crystals. The data for Fe_2Ge_3 polycrystals are included for comparison [28,30]. (b) Low-temperature resistivity of Fe_2Ge_3 crystals. The red line is the fit using Eqs. (1) and (2). The contributions from electron-electron scattering, Einstein modes, and electron-phonon scattering are colored with gray, green, and magenta, respectively. The uncertainty of resistivity is 6%.

resistance ratio (RRR $= \rho_{300\,\mathrm{K}}/\rho_{2\,\mathrm{K}}$) ≈ 233 for sample S1. Different from our observations, the resistivity of a polycrystal reported by Verchenko *et al.* [30] decreases with increasing temperature and shows an obvious semiconducting behavior. This discrepancy may come from the different stoichiometric ratio in the samples and the resistivity due to the extrinsic impurity band in the polycrystalline sample. [30] The resistivity data below 50 K can be fitted using the following equation [37]:

$$\rho(T) = \rho_0 + \rho_{\mathrm{Einstein}}(T) + AT^2 + BT^5, \tag{1}$$

where ρ_0 is the residual resistivity, $\rho_{\mathrm{Einstein}}(T)$ is the contribution from the Einstein mode, and A and B are coefficients for electron-electron scattering and electron-phonon scattering, respectively. It was found that the contribution of an Einstein mode to the resistivity can be described by [38]

$$\rho_{\mathrm{Einstein}}(T) = \frac{KN}{MT\exp\left(\frac{\theta_E}{T}-1\right)\left[1-\exp\left(\frac{-\theta_E}{T}\right)\right]}, \tag{2}$$

where M is the mass of the oscillator, N is the number of oscillators per unit volume, K is a parameter dependent on the electron density and the strength of the coupling between electrons and local phonon modes, and θ_E is the characteristic temperature of the Einstein mode. As shown in Fig. 5(b), the measured ρ can be fitted well with the model. The θ_E obtained from the fitting is 61 K. The electron-electron scattering dominates at low temperatures with the electron-electron scattering coefficient of 1.12 μΩ cm K^{-2}. Above 350 K, the resistivity exhibits a decreasing tendency with temperature due to the thermal excitation of electron-hole pairs. Therefore, we fit the high-temperature resistivity data using the following equation:

$$\rho(T) = C\exp\left(\frac{E_g}{k_B T}\right), \tag{3}$$

where C is residual resistivity, E_g is band gap energy, and k_B is Boltzmann's constant. An Arrhenius plot of resistivity is shown in Fig. S4 [36] with a narrow band gap energy of 0.03 eV. This band gap is in agreement with the reported value determined from the resistivity data of a polycrystal sample ($E_g = 0.03$ eV). [30] It is noted that sample S2 has a much larger residual resistivity and shows a slight decrease in resistivity with increasing temperature below 10 K (Fig. S5 in the SM [36]), which could be attributed to a stronger electron-impurity scattering. In addition, distribution of commensurate and incommensurate structures could also affect the resistivity of Fe_2Ge_3, which deserves further investigation.

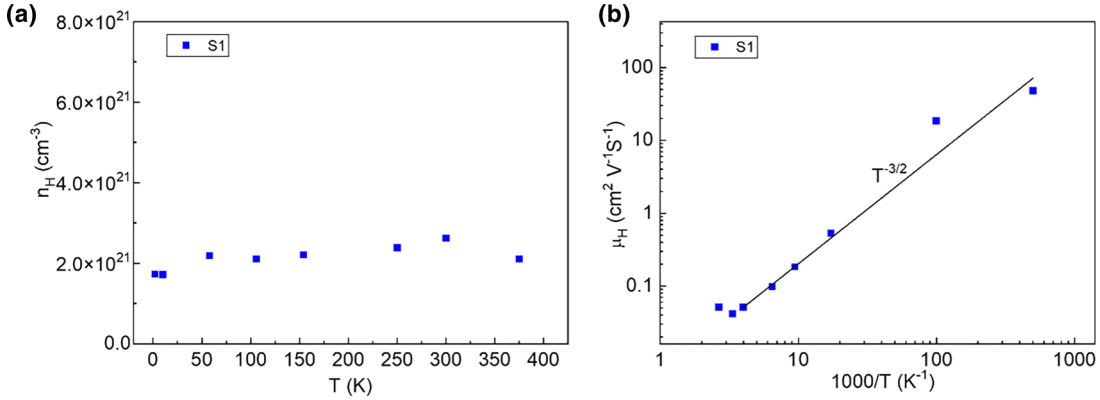

FIG. 6. (a) Hall carrier concentration and (b) mobility of a Fe_2Ge_3 crystal as a function of temperature. The uncertainty of Hall carrier concentration is 6% and the uncertainty of mobility is 8%.

TABLE III. Experimentally measured physical properties of Fe_2Ge_3 (S1) at 300 K.

S	σ	n_H	μ_H	C_p	θ_D	v_m	κ
(μV K^{-1})	(Ω^{-1} cm^{-1})	(10^{21} cm^{-3})	(cm^2 V^{-1} S^{-1})	(J mol^{-1} K^{-1})	(K)	(m s^{-1})	(W m^{-1} K^{-1})
−141	15	2.5	0.037	112 (250 K)	325	4175	1.9

Figures 6(a) and 6(b) show the Hall carrier concentration and mobility of Fe_2Ge_3 as a function of temperature, respectively. The electron concentration is essentially independent of temperature, which is characteristic of a degenerate semiconductor. [39] The Hall voltage as a function of magnetic field at 300 K is shown in Fig. S6 with a negative slope, verifying its n-type semiconducting behavior. The mobility of Fe_2Ge_3 varies approximately as $T^{-3/2}$ above 50 K. This result indicates that acoustic phonon scattering is the dominant carrier scattering mechanism in Fe_2Ge_3 single crystals. [40] Table III summarizes the Hall carrier concentration and mobility, along with other physical properties of Fe_2Ge_3 at room temperature.

Figure 7 shows the temperature dependence of the Seebeck coefficient of Fe_2Ge_3 single crystals, measured with a temperature gradient along the c axis. The Seebeck coefficient is negative and its magnitude increases linearly with temperature. This behavior is expected for a degenerate or heavily doped n-type semiconductor, which agrees with the Hall measurement results discussed earlier.

In general, NCL phases composed of transition metals are stable if the valence electron count (VEC) per number of transition metals is around 14. [41,42] The compound is a semiconductor when the VEC is equal to 14. A qualitative explanation for this empirical principle is that the T atoms in NCLs T_mE_n need to achieve a filled 18-electron configuration through the covalent sharing of electron pairs at four T-T contacts around each T atom. In this way, filled 18-electron configurations only require 14 electrons per T atom. [43] For n-type materials, the VEC is larger than 14 and an increase of VEC above 14 corresponds to a shift in Fermi level away from the conduction band bottom. VEC is linked to the atomic ratio of Ge:Fe(δ) via VEC $= 8 + 4\delta$ because each Fe atom has eight valence electrons, and each Ge atom has four valence electrons. [44] Furthermore, the charge carrier density can be approximated by calculating the number of conduction electrons within the Fe sublattice. The number of conduction electrons per Fe atom is calculated as (VEC–14), which is equal to the difference between the valence electrons and the number of paired electrons per Fe atom. Given that the Fe sublattice in a Fe_2Ge_3 unit cell contains four Fe atoms, the charge carrier density can be estimated by [33]

$$n = \frac{4(\mathrm{VEC} - 14)}{v_{\mathrm{Fe}}} = \frac{4(4\delta - 6)}{v_{\mathrm{Fe}}}, \tag{4}$$

where v_{Fe} is the volume of the Fe sublattice in the unit cell. Using Eq. (4) and the experimental electron density from the Hall measurements and lattice parameters from XRD data, δ is calculated to be 1.517 with a corresponding VEC of 14.068. This value is close to the value determined by SCXRD.

The Seebeck coefficient of a heavily doped semiconductor is given by [45,46]

$$S = \frac{8\pi^{8/3}k_B^2\left(r + \frac{3}{2}\right)m_d^*}{3^{5/3}eh^2\,n^{2/3}}T, \tag{5}$$

where h is Planck's constant, m^* is the density of states effective mass, and r is the scattering parameter, which is zero when acoustic phonon scattering is the dominant scattering mechanism. The extracted effective mass of Fe_2Ge_3 is about $7.3m_0$, where m_0 is the free electron mass. This value is smaller than that of $MnSi_{1.74}$ ($9m_0$). [39]

In previous studies, [10,47] it has been found that the TE properties of NCL phases are highly anisotropic due to their unique crystal structures. It is expected that the Fe_2Ge_3 crystals may also exhibit a similar anisotropic behavior. However, our crystals are not large enough for the TE property measurements perpendicular to the c axis. Efforts are required to improve the growth method in order to increase the size of the crystals. In addition, it is noticed that the PF and zT of the single crystals are 0.03 mW m^{-1} K^{-2} and 0.005 at 300 K, respectively, both of which are low as compared to other TE materials. [48,49] A zT of 0.3 at 373 K has been reported for polycrystalline Fe_2Ge_3. [28] The low zT in our sample is primarily attributed to its lower electrical conductivity. The previous first-principles calculations by Sato *et al.* [28] have demonstrated that the zT value over unity at 600 K can be achieved by doping. Further work is needed to improve the thermoelectric properties of Fe_2Ge_3 crystals by doping.

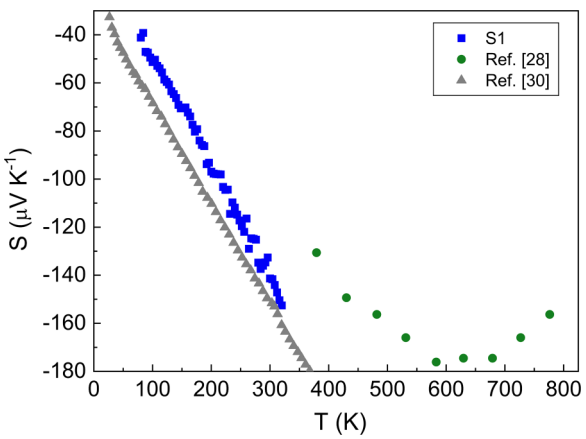

FIG. 7. Temperature dependence of the Seebeck coefficient of a Fe_2Ge_3 crystal measured along the c axis. The data from Sato *et al.* [28] and Verchenko *et al.* [30] are included for comparison. The uncertainty of the Seebeck coefficient is 5%.

D. Thermal properties

Temperature dependence of the specific heat of Fe_2Ge_3 in the temperature range of 1.9–250 K is shown in Fig. 8. No sign of any phase transition is observed in this temperature range. According to Fig. 8(a), the specific heat at 250 K attains a value of 112 J mol^{-1} K^{-1}, which is slightly smaller than

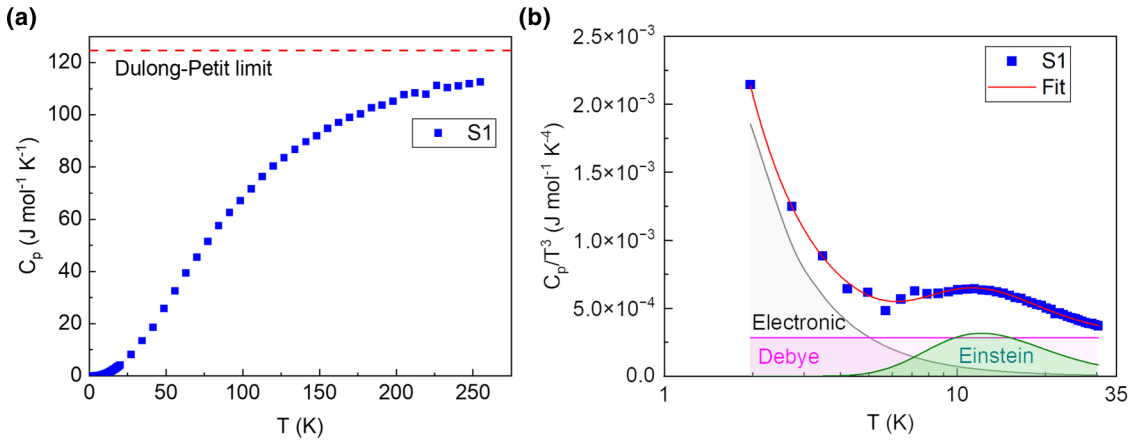

FIG. 8. (a) Temperature dependence of specific heat in the temperature range of 1.9–250 K. The red dashed line is the Dulong-Petit limit. (b) Temperature dependence of C_p/T^3 below 30 K. The solid red line shows the fitting as described in the text. Specific heat contributions from electronic, Debye, and Einstein terms are labeled in gray, magenta, and green, respectively.

the classical high-temperature Dulong-Petit value of $3nR = 125\,\mathrm{J\,mol^{-1}\,K^{-1}}$ at constant volume, where R is the molar gas constant and $n = 5$ is the number of atoms per formula unit. Figure 8(b) shows the temperature dependence of C_p/T^3 below 30 K. The weak hump around 12 K suggests the presence of an Einstein mode due to low-energy optic modes. This bump has also been observed in glasslike materials. [50] The solid red line in Fig. 8(b) represents the fitting including electronic specific heat, Debye term, and Einstein term using the following equation [51]:

$$\frac{C_p}{T^3} = \frac{\gamma}{T^2} + \frac{12\pi^4 N k_B}{5\theta_D^3} + n_E R \frac{\theta_E^2}{T^5} \frac{e^{\theta_E/T}}{(e^{\theta_E/T} - 1)^2}, \qquad (6)$$

where γ is the electronic specific heat coefficient, N is the number of atoms per mole, θ_D is the Debye temperature, and n_E is the Einstein oscillator strength per mole. The fitting leads to a γ of $0.00718\,\mathrm{J\,mol^{-1}\,K^{-2}}$, a θ_D of 325 K, a θ_E of 59.7 K, and a n_E of 0.38. The obtained Einstein temperature with a corresponding energy of about 5 meV matches well with the value from the resistivity analysis. According to the fitting of resistivity and specific heat data, the electron-electron scattering coefficient A is $1.12\,\mu\Omega\,\mathrm{cm\,K^{-2}}$ and the Sommerfeld value of the specific heat γ is $7.18\,\mathrm{mJ\,mol^{-1}\,K^{-2}}$. The Kadowaki-Woods ratio (A/γ^2) is calculated to be $2.17 \times 10^4\,\mu\Omega\,\mathrm{cm\,mol^2\,K^2\,J^{-2}}$. This value is much larger than transition metals and many heavy-fermion compounds, [52] indicating strong electron correlations in the compound. The sound velocity (v_s) was calculated using the following equation:

$$v_s = \frac{k_B \theta_D}{\hbar} \left(\frac{6\pi^2 N}{V} \right)^{-1/3}, \qquad (7)$$

where V is the volume of the unit cell. The calculated value is $4175\,\mathrm{m\,s^{-1}}$. Notably, the sound velocity of Fe_2Ge_3 is smaller than that of $MnSi_{1.74}$, which is $5095\,\mathrm{m\,s^{-1}}$. [39]

In order to better understand the thermal transport in Fe_2Ge_3, we measured the thermal conductivity of a Fe_2Ge_3 single crystal with a temperature gradient along the c axis, as shown in Fig. 9. The measured value is about $1.9\,\mathrm{W\,m^{-1}\,K^{-1}}$ at 300 K, which is smaller than that of $MnSi_{1.74}$ along the c axis ($2.3\,\mathrm{W\,m^{-1}\,K^{-1}}$). The lower thermal conductivity in Fe_2Ge_3 can be attributed to its lower sound velocity as discussed above. The electronic thermal conductivity can be estimated by $\kappa_E = LT/\rho$, where L is the Lorenz number. The value of L is determined to be $1.8 \times 10^{-8}\,\mathrm{V^2\,K^{-2}}$, according to an equation considering a single parabolic band with acoustic phonon scattering as $L = 1.5 + e^{-|S|/116}$. [53] The calculated κ_E is $0.0024\,\mathrm{W\,m^{-1}\,K^{-1}}$ at 300 K, which is negligible as compared to the total thermal conductivity due to the relatively high resistivity. The measured thermal conductivity shows a plateau in the temperature range from 50 to 300 K. Li *et al.* [29] conducted first-principles calculations of phonon dispersions and thermal transport in Fe_2Ge_3. They observed some low-lying optical phonon modes with energies of 1.8 meV at the Brillouin zone center, which exhibit avoided crossings with longitudinal acoustic phonons. In addition,

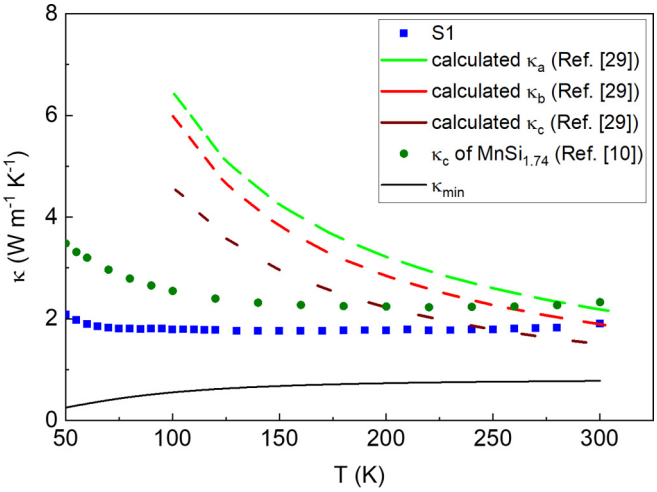

FIG. 9. Temperature dependence of the total thermal conductivity of a Fe_2Ge_3 crystal measured along the c axis. The uncertainty of thermal conductivity is 15%. The three dashed lines are the calculated thermal conductivities of Fe_2Ge_3 along three crystallographic axes using the first-principles method [29]. Thermal conductivity of $MnSi_{1.74}$ along the c axis is also shown for comparison [10].

another optical branch with energy of 5 meV at the zone center was observed. As a result, the optical-acoustic phonon coupling can increase phonon scattering rates and reduce lattice thermal conductivity. According to our resistivity and specific heat analysis, low-lying optical modes with energy of 5 meV are present in Fe_2Ge_3, which is consistent with the calculations. These optical phonons can scatter heat-carrying acoustic phonons and reduce lattice thermal conductivity of Fe_2Ge_3. However, it should be noted that our experimental data show a much weaker temperature dependence than the model predicts. As the model is based on the phonon transport model, other mechanisms could contribute to the thermal transport behavior of Fe_2Ge_3. In complex crystal structures, thermal transport involves degenerate overlapping optical vibrational modes that participate through a hopping mechanism, distinct from the gaslike phonons. These modes are referred to as "diffusons." [54] A two-channel model including a phonon channel and a diffuson channel has been proposed for materials with low lattice thermal conductivity. [55–57] A similar low thermal conductivity along the c axis has been reported in single crystals of NCL $MnSi_{1.74}$, as shown in Fig. 9, and is described by the two-channel model. [10] It has been found that the phonon contribution to thermal conductivity deceases with the temperature while the diffuson contribution increases with the temperature, leading to a weak temperature dependence in $MnSi_{1.74}$. Such a two-channel model could also be used to explain the intrinsic low thermal conductivity in Fe_2Ge_3 in this work.

The minimum thermal conductivity ($\kappa_{\min}$) of Fe_2Ge_3 can be calculated according to the model developed by Cahill *et al.* [58] with the following equation:

$$\kappa_{\min} = \left(\frac{\pi}{6}\right)^{1/3} k_B n_A^{2/3} v_s \left(\frac{T}{\theta}\right)^2 \int_0^{\theta/T} \frac{x^3 e^x}{(e^x - 1)^2} dx, \qquad (8)$$

where n_A is the density of atoms. The $\kappa_{\min}$ of Fe_2Ge_3 was calculated to be $0.78\,W\,m^{-1}\,K^{-1}$ at 300 K. Therefore, the thermal conductivity of Fe_2Ge_3 can be further suppressed by increasing the phonon-boundary scattering via ball milling [23] and phonon-impurity scattering via chemical doping. [59] Indeed, a low thermal conductivity of $0.85\,W\,m^{-1}\,K^{-1}$ at 300 K was reported in a polycrystalline Fe_2Ge_3 sample. [30] Regarding the diffuson thermal transport, it has been demonstrated that its contribution can be decreased by increasing the energetic spacing between vibrational modes. [57] Therefore, proper dopants can be used to modify the phonon dispersion of Fe_2Ge_3 and increase overlapping of phonon modes associated with different atoms.

IV. CONCLUSION

We synthesized the single crystalline NCL compound Fe_2Ge_3 and conducted a comprehensive characterization of its intrinsic physical properties. The temperature-independent magnetic susceptibility could be attributed to Pauli paramagnetism by conduction electrons. The Seebeck coefficient of Fe_2Ge_3 is negative and its magnitude increases linearly with temperature, which indicates that the obtained Fe_2Ge_3 is a degenerate n-type semiconductor with an electron effective mass of $7.3m_0$. The analysis of low-temperature resistivity and specific heat data reveals an Einstein mode with a characteristic temperature of about 60 K, corresponding to low-energy optical phonon modes with an energy of 5 meV. The high-temperature resistivity fitting with the Arrhenius law indicates a narrow band gap of 0.03 eV. Furthermore, the thermal conductivity of Fe_2Ge_3 along the c axis shows a temperature-independent behavior with an intrinsically low value of $1.9\,W\,m^{-1}\,K^{-1}$ at 300 K. Such a low thermal conductivity can be attributed to the scattering of acoustic phonons by low-energy optical modes. In addition, it is possible that diffusons contribute to thermal transport in Fe_2Ge_3 as reported in another NCL phase $MnSi_{1.74}$, [10] leading to a thermal conductivity plateau in a wide temperature range. Our results provide important insights into the origin of the intrinsic low thermal conductivity in Fe_2Ge_3 and can enable further studies on enhancing its TE performance.

ACKNOWLEDGMENTS

The authors would like to thank Andrew May for discussions and Jianshi Zhou for the help with thermoelectric property measurements. This work was supported by the National Science Foundation (NSF) under Grant No. 2144328. X.C. acknowledges financial support from the University of California, Riverside. Work at ORNL was supported by the U.S. Department of Energy, Office of Science, Basic Energy Sciences, Materials Sciences and Engineering Division. This research used resources at the Spallation Neutron Source, a DOE Office of Science User Facility operated by ORNL.

[1] F. J. DiSalvo, Science **285**, 703 (1999).
[2] B. C. Sales, Science **295**, 1248 (2002).
[3] X. Shi and J. He, Science **371**, 343 (2021).
[4] H. Hohl, A. P. Ramirez, C. Goldmann, G. Ernst, B. Wölfing, and E. Bucher, J. Phys.: Condens. Matter **11**, 1697 (1999).
[5] G. Joshi, H. Lee, Y. Lan, X. Wang, G. Zhu, D. Wang, R. W. Gould, D. C. Cuff, M. Y. Tang, M. S. Dresselhaus *et al.*, Nano Lett. **8**, 4670 (2008).
[6] S. I. Kim, K. H. Lee, H. A. Mun, H. S. Kim, S. W. Hwang, J. W. Roh, D. J. Yang, W. H. Shin, X. S. Li, Y. H. Lee *et al.*, Science **348**, 109 (2015).
[7] D. M. Rowe, V. S. Shukla, and N. Savvides, Nature **290**, 765 (1981).
[8] L. Hu, T. Zhu, X. Liu, and X. Zhao, Adv. Funct. Mater. **24**, 5211 (2014).
[9] Y. Xu, Z. Barani, P. Xiao, S. Sudhindra, Y. Wang, A. A. Rezaie, V. Carta, K. N. Bozhilov, D. Luong, B. P. T. Fokwa *et al.*, Chem. Mater. **34**, 8858 (2022).
[10] X. Chen, A. Weathers, J. Carrete, S. Mukhopadhyay, O. Delaire, D. A. Stewart, N. Mingo, S. N. Girard, J. Ma, D. L. Abernathy *et al.*, Nat. Commun. **6**, 6723 (2015).
[11] L. D. Zhao, G. Tan, S. Hao, J. He, Y. Pei, H. Chi, H. Wang, S. Gong, H. Xu, V. P. Dravid *et al.*, Science **351**, 141 (2016).

[12] L. D. Zhao, S. H. Lo, Y. Zhang, H. Sun, G. Tan, C. Uher, C. Wolverton, V. P. Dravid, and M. G. Kanatzidis, Nature **508**, 373 (2014).

[13] G. J. Snyder and E. S. Toberer, Nat. Mater. **7**, 105 (2008).

[14] H. Xie, S. Hao, J. Bao, T. J. Slade, G. J. Snyder, C. Wolverton, and M. G. Kanatzidis, J. Am. Chem. Soc. **142**, 9553 (2020).

[15] W. Li, S. Lin, M. Weiss, Z. Chen, J. Li, Y. Xu, W. G. Zeier, and Y. Pei, Adv. Energy Mater. **8**, 1800030 (2018).

[16] J. M. Higgins, A. L. Schmitt, I. A. Guzei, and S. Jin, J. Am. Chem. Soc. **130**, 16086 (2008).

[17] V. Ponnambalam and D. T. Morelli, J. Electron. Mater. **41**, 1389 (2012).

[18] I. Aoyama, H. Kaibe, L. Rauscher, T. Kanda, M. Mukoujima, S. Sano, and T. Tsuji, Jpn. J. Appl. Phys. **44**, 4275 (2005).

[19] Y. Arita, S. Mitsuda, Y. Nishi, T. Matsui, and T. Nagasaki, J. Nucl. Mater. **294**, 202 (2001).

[20] V. Ponnambalam, G. Lehr, and D. T. Morelli, J. Mater. Res. **26**, 1907 (2011).

[21] M. Hayward, A. Ramirez, and R. Cava, J. Solid State Chem. **166**, 389 (2002).

[22] A. Yamamoto, S. Ghodke, H. Miyazaki, M. Inukai, Y. Nishino, M. Matsunami, and T. Takeuchi, Jpn. J. Appl. Phys. **55**, 020301 (2016).

[23] X. Chen, A. Weathers, D. Salta, L. Zhang, J. Zhou, J. B. Goodenough, and L. Shi, J. Appl. Phys. **114**, 173705 (2013).

[24] X. Chen, J. Zhou, J. B. Goodenough, and L. Shi, J. Mater. Chem. C **3**, 10500 (2015).

[25] K. B. Gerasimov and S. V. Pavlov, Intermetallics **8**, 451 (2000).

[26] W. Li, Y. Li, X. Ma, and Z. Zhang, Mater. Chem. Phys. **148**, 490 (2014).

[27] T. Terada, R. Kitaura, S. Ishigaki, T. Ishibe, N. Naruse, Y. Mera, R. Asahi, and Y. Nakamura, Acta Mater. **236**, 118130 (2022).

[28] N. Sato, H. Ouchi, Y. Takagiwa, and K. Kimura, Chem. Mater. **28**, 529 (2016).

[29] W. Li, J. Carrete, G. K. H. Madsen, and N. Mingo, Phys. Rev. B **93**, 205203 (2016).

[30] V. Y. Verchenko, Z. Wei, A. A. Tsirlin, C. Callaert, A. Jesche, J. Hadermann, E. V. Dikarev, and A. V. Shevelkov, Chem. Mater. **29**, 9954 (2017).

[31] C. Chien, *The Hall Effect and its Applications* (Springer Science & Business Media, Berlin, 2013).

[32] F. Tian, B. Song, X. Chen, N. K. Ravichandran, Y. Lv, K. Chen, S. Sullivan, J. Kim, Y. Zhou, T.-H. Liu *et al.*, Science **361**, 582 (2018).

[33] S. Le Tonquesse, C. Hassam, Y. Michiue, Y. Matsushita, M. Pasturel, T. Mori, T. S. Suzuki, and D. Berthebaud, J. Alloys Compd. **846**, 155696 (2020).

[34] X. Chen, K. Jarvis, S. Sullivan, Y. T. Li, J. Zhou, and L. Shi, Phys. Rev. B **95**, 144310 (2017).

[35] J. Rodríguez-Carvajal, Physica B (Amsterdam) **192**, 55 (1993).

[36] See Supplemental Material at http://link.aps.org/supplemental/10.1103/PhysRevMaterials.7.125404 for additional details and figures on experiments.

[37] M. J. Winiarski and T. Klimczuk, J. Solid State Chem. **245**, 10 (2017).

[38] J. R. Cooper, Phys. Rev. B **9**, 2778 (1974).

[39] X. Chen, S. N. Girard, F. Meng, E. Lara-Curzio, S. Jin, J. B. Goodenough, J. Zhou, and L. Shi, Adv. Energy Mater. **4**, 1400452 (2014).

[40] J. Bardeen and W. Shockley, Phys. Rev. **80**, 72 (1950).

[41] Y. Imai and A. Watanabe, Intermetallics **13**, 233 (2005).

[42] D. C. Fredrickson, S. Lee, and R. Hoffmann, Inorg. Chem. **43**, 6159 (2004).

[43] V. J. Yannello and D. C. Fredrickson, Inorg. Chem. **53**, 10627 (2014).

[44] Y. Miyazaki and Y. Kikuchi, in *Thermoelectric Nanomaterials: Materials Design and Applications*, edited by K. Koumoto and T. Mori (Springer, Berlin, 2013), p. 141.

[45] J. Xing, X. Chen, Y. Y. Zhou, J. C. Culbertson, J. A. Freitas, E. R. Glaser, J. S. Zhou, L. Shi, and N. Ni, Appl. Phys. Lett. **112**, 261901 (2018).

[46] T. Hosseini, N. Yavarishad, J. Alward, N. Kouklin, and M. Gajdardziska-Josifovska, Adv. Electron. Mater. **2**, 1500319 (2016).

[47] N. S. Chauhan, I. Ono, K. Hayashi, and Y. Miyazaki, J. Alloys Compd. **935**, 167983 (2023).

[48] J. P. Heremans, V. Jovovic, E. S. Toberer, A. Saramat, K. Kurosaki, A. Charoenphakdee, S. Yamanaka, and G. J. Snyder, Science **321**, 554 (2008).

[49] M. Scheele, N. Oeschler, K. Meier, A. Kornowski, C. Klinke, and H. Weller, Adv. Funct. Mater. **19**, 3476 (2009).

[50] A. P. Sokolov, R. Calemczuk, B. Salce, A. Kisliuk, D. Quitmann, and E. Duval, Phys. Rev. Lett. **78**, 2405 (1997).

[51] Y. Li, H. Y. Bai, W. H. Wang, and K. Samwer, Phys. Rev. B **74**, 052201 (2006).

[52] A. C. Jacko, J. O. Fjærestad, and B. J. Powell, Nat. Phys. **5**, 422 (2009).

[53] H.-S. Kim, Z. M. Gibbs, Y. Tang, H. Wang, and G. J. Snyder, APL. Mater. **3**, 041506 (2015).

[54] P. B. Allen, J. L. Feldman, J. Fabian, and F. Wooten, Philos. Mag. B **79**, 1715 (1999).

[55] M. T. Agne, T. Böger, T. Bernges, and W. G. Zeier, PRX Energy **1**, 031002 (2022).

[56] S. Mukhopadhyay, D. S. Parker, B. C. Sales, A. A. Puretzky, M. A. McGuire, and L. Lindsay, Science **360**, 1455 (2018).

[57] R. Hanus, J. George, M. Wood, A. Bonkowski, Y. Cheng, D. L. Abernathy, M. E. Manley, G. Hautier, G. J. Snyder, and R. P. Hermann, Mater. Today Phys. **18**, 100344 (2021).

[58] D. G. Cahill, S. K. Watson, and R. O. Pohl, Phys. Rev. B **46**, 6131 (1992).

[59] X. Chen, L. Shi, J. Zhou, and J. B. Goodenough, J. Alloys Compd. **641**, 30 (2015).